

Anisotropic Diffusion in Vector Field Visualization on Euclidian Domains and Surfaces

U. Diewald, T. Preußer, M. Rumpf*

Abstract

Vector field visualization is an important topic in scientific visualization. Its aim is to graphically represent field data on two and three-dimensional domains and on surfaces in an intuitively understandable way. Here a new approach based on anisotropic nonlinear diffusion is introduced. It enables an easy perception of vector field data and serves as an appropriate scale space method for the visualization of complicated flow pattern. The approach is closely related to nonlinear diffusion methods in image analysis where images are smoothed while still retaining and enhancing edges. Here an initial noisy image intensity is smoothed along integral lines, whereas the image is sharpened in the orthogonal direction. The method is based on a continuous model and requires the solution of a parabolic PDE problem. It is discretized only in the final implementational step. Therefore, many important qualitative aspects can already be discussed on a continuous level. Applications are shown for flow fields in 2D and 3D as well as for principal directions of curvature on general triangulated surfaces. Furthermore the provisions for flow segmentation are outlined.

Keywords: flow visualization, multiscale, nonlinear diffusion, segmentation

1 Introduction

The visualization of field data, especially of velocity fields from CFD computations is one of the fundamental tasks in scientific visualization. A variety of different approaches has been presented. The simplest method to draw vector plots at nodes of some overlaid regular grid in general produces visual clutter, because of the typically different local scaling of the field in the spatial domain, which leads to disturbing multiple overlaps in certain regions, whereas in other areas small structures such as eddies can not be resolved adequately. This gets even worse if tangential fields on highly curved surfaces are considered.

The central goal is to come up with intuitively better receivable methods, which give an overall as well as detailed view on the flow patterns. Single particle lines only very partially enlighten features of a complex flow field. Thus, we want to define a texture which represents the field globally on a 2D or 3D domain and on surfaces respectively. Here we confine ourselves to stationary fields. In the Euclidian case we suppose $v : \Omega \rightarrow \mathbb{R}^n$ for some domain $\Omega \subset \mathbb{R}^n$, whereas in case of a manifold \mathcal{M} embedded in \mathbb{R}^3 we consider a tangential vector field v . We ask for a method generating stretched streamline type patterns, which are aligned to the vector field $v(x)$. Furthermore, the possibility to successively coarsen this pattern is obviously an desirable property. Methods which are based on such a scale of spaces and enhance certain structures of images are well known in image processing analysis. Actually nonlinear diffusion allows the smoothing of grey or color images while retaining and enhancing edges [18]. Now we set up a diffusion problem, with strong smoothing along integral lines and edge enhancement in the

orthogonal directions. Applying this to some initial random noise image intensity we generate a scale of successively coarser patterns which represent the vector field. Finite elements in space and a semi implicit time stepping are applied to solve this diffusion problem numerically. Furthermore a suitable modification of the approach allows the identification of topological regions.

Before we explain in detail the method, let us discuss related work on vector field visualization and image processing. Later on we will identify some of the well known methods as equivalent to special cases, or asymptotic limits of the presented new method respectively.

2 Related work

The spot noise method proposed by van Wijk [25] introduces spot like texture splats which are aligned by deformation to the velocity field in 2D or on surfaces in 3D. These splats are plotted in the fluid domain showing strong alignment patterns in the flow direction. The originally first order approximation to the flow was improved by de Leeuw and van Wijk in [6] by using higher order polynomial deformations of the spots in areas of significant vorticity. In an animated sequence these spots can be moved along streamlines of the flow. Furthermore in 3D van Wijk [26] applies the integration to clouds of oriented particles and animates them by drawing similar moving transparent and illuminated splats.

The Line Integral Convolution (LIC) approach of Cabral and Leedom [4] integrates the fundamental ODE describing streamlines forward and backward in time at every pixelized point in the domain, convolves a white noise along these particle paths with some Gaussian type filter kernel, and takes the resulting value as an intensity value for the corresponding pixel. According to the strong correlation of this intensity along the streamlines and the lack of any correlation in the orthogonal direction the resulting texturing of the domain shows dense streamline filaments of varying intensity. Hege and Stalling [21] increased the performance of this method especially by reusing portions of the convolution integral already computed on points along the streamline. Forssell [10] proposed a similar method on surfaces and Max et al. [17] discuss flow visualization by texturing on contour surfaces. Max and Becker [16] presented a method for visualizing 2D and 3D flows by animating textures.

Shen and Kao [20] applied a LIC type method to unsteady flow fields. Recently a method [2] has been presented, which generates streakline type patterns by numerical calculation of the transport of inlet coordinates and inlet position. Interrante and Grosch [12] generalized line integral convolution to 3D in terms of volume rendering of line filaments.

In [24] Turk discusses an approach which selects a certain number of streamlines. They are automatically equally distributed all over the computational domain to characterize in a sketch type representation the significant aspects of the flow. An energy minimizing process is used to generate the actual distribution of streamlines.

Especially for 3D velocity fields particle tracing is a very popular tool. But a few particle integrations released by the user can hardly scope with the complexity of 3D vector fields. Zöckler et

* Institute for Applied Mathematics, University of Bonn, Wegelerstraße 6, 53115 Bonn, Germany, [*diewald | tpreuss | rumpf*]@iam.uni-bonn.de

al. [22] use pseudo randomly distributed, illuminated and transparent streamlines to give a denser and more perceptible representation, which shows the overall structure and enhances important details. Van Wijk [27] proposed the implicit stream surface method. For a stationary flow field the transport equations $v \cdot \nabla \phi = 0$ are solved for given v and certain inflow and outflow boundary conditions in a pre-computing step. Then isosurfaces of the resulting function ϕ are streamsurfaces and can efficiently be extracted with interactive frame rates even for larger data sets.

Most of the methods presented so far have in common, that the generation of a coarser scale requires a recomputation. For instance, if we ask for a finer or coarser scale of the line integral convolution pattern, the computation has to be restarted with a coarser initial image intensity. In case of spot noise larger spots have to be selected and their stretching along the field has to be increased. The approach to be presented here will incorporate a successive coarsening as time proceeds in the underlying diffusion problem.

As already mentioned in the introduction our method of anisotropic nonlinear diffusion to visualize vector fields is derived from well known image processing methodology. Discrete diffusion type methods are known for a long time. Perona and Malik [18] have introduced a continuous diffusion model which allows the denoising of images together with the enhancing of edges. Alvarez, Guichard, Lions and Morel [1] have established a rigorous axiomatic theory of diffusive scale space methods. Kawohl and Kutev [14] investigate a qualitative analysis of the Perona and Malik model. The recovering of lower dimensional structures in images is analyzed by Weickert [28], who introduced an anisotropic nonlinear diffusion method where the diffusion matrix depends on the so called structure tensor of the image. A finite element discretization and its convergence properties have been studied by Kačur and Mikula [13].

Concerning the application of diffusion type methods on surfaces, a general introduction to differential calculus on manifolds can be found for instance in the book by do Carmo [7]. Dziuk [8] presents an algorithm for the solution of partial differential equations on surfaces and in [9] he discusses a numerical method for geometric diffusion applied to the surface itself, which coincides with the mean curvature motion.

3 The nonlinear diffusion problem

Let us now derive our method based on a suitable PDE problem. At first, we confine ourselves to the case of planar domains in 2D and 3D. Here, nonlinear anisotropic diffusion applied to some initial random noisy image will enable an intuitive and scalable visualization of complicated vector fields. Therefore, we pick up the idea of line integral convolution, where a strong correlation in the image intensity along integral lines is achieved by convolution of an initial white noise along these lines. As proposed already by Cabral and Leedom [4] a suitable choice for the convolution kernel is a Gaussian kernel. On the other hand an appropriately scaled Gaussian kernel is known to be the fundamental solution of the heat equation. Thus, line integral convolution is nothing else than solving the heat equation in 1D on an integral line parameterized with respect to arc length. On pixels which are located on different integral lines the resulting image intensities are not correlated. Hence, the thickness of the resulting image patterns in line integral convolution is of the size of the random initial patterns, in general a single pixel. Increasing this size as it has been proposed by Kiu and Banks [15] leads to broader stripes and unfortunately less sharp transitions across streamline patterns. As described so far, line integral convolution is a discrete pixel based method. If we ask for a well posed continuous diffusion problem with similar properties, we are lead to some anisotropic diffusion, now controlled by a suitable diffusion matrix.

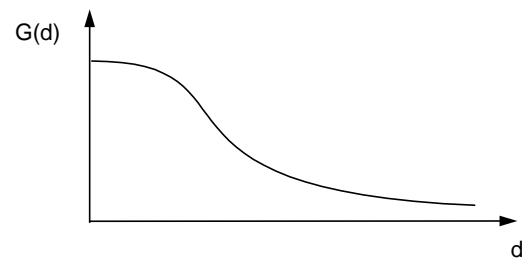


Figure 1: The shape $G(\cdot)$ which applied to the gradient of the mollified image intensity serves as a diffusion coefficient in image processing.

To begin with, let us at first introduce a general nonlinear diffusion method from image processing and then discuss the selection of the appropriate diffusion tensor and the right hand side. Here we consider first the case of an image in Euclidian space either in 2D or 3D. In Section 6 we then generalize this with respect to textures on surfaces. We consider a function $\rho : \mathbb{R}_0^+ \times \Omega \rightarrow \mathbb{R}$ which solves the parabolic problem

$$\begin{aligned} \frac{\partial}{\partial t} \rho - \operatorname{div}(A(\nabla \rho_\epsilon) \nabla \rho) &= f(\rho) && \text{in } \mathbb{R}^+ \times \Omega, \\ \rho(0, \cdot) &= \rho_0 && \text{on } \Omega, \\ \frac{\partial}{\partial \nu} \rho &= 0 && \text{on } \mathbb{R}^+ \times \partial \Omega \end{aligned}$$

for given initial density $\rho_0 : \Omega \rightarrow [0, 1]$. Here $\rho_\epsilon = \chi_\epsilon * \rho$ is a mollification of the current density, which will later on turn out to be necessary for the wellposedness of the above parabolic, boundary and initial value problem. In our setting we interpret the density as an image intensity, a scalar greyscale or – with a slight extension to the vector valued case – as a vector valued color. Thus, the solution $\rho(\cdot)$ can be regarded as a family of images $\{\rho(t)\}_{t \in \mathbb{R}_0^+}$, where the time t serves as a scaling parameter. Let us remark, that by the trivial choice $A = 1$ and $f(\rho) = 0$ we obtain the standard linear heat equation with its isotropic smoothing effect. In image processing ρ_0 is a given noisy initial image. The diffusion is supposed to be controlled by the gradient of the image intensity. Large gradients mark edges in the image, which should be enhanced, whereas small gradients indicate areas of approximately equal intensity. Here denoising, i. e. intensity diffusion is considered. For that purpose we prescribe a diffusion coefficient

$$A = G(\|\nabla \rho_\epsilon\|)$$

where $G : \mathbb{R}_0^+ \rightarrow \mathbb{R}^+$ is a monotone decreasing function with $\lim_{d \rightarrow \infty} G(d) = 0$ and $G(0) = \beta$ where $\beta \in \mathbb{R}^+$ is constant (cf. Fig. 1), e. g. $G(d) = \frac{\beta}{1 + \|d\|^2}$. If we would replace the mollified gradient $\nabla \rho_\epsilon$ as argument of G by the true gradient $\nabla \rho$, which leads to the original Perona Malik model, we would in general obtain a backward parabolic problem in areas of high gradients, which is no longer well posed [14]. The invoked mollification avoids this shortcoming and comes along with a desirable presmoothing effect. Nevertheless the enhancing of steep gradients and thereby edges in the image, known from backward diffusion is retained if we adjust the mollification carefully. A suitable choice [13] for this mollification is a convolution with the heat equation kernel. I.e. we define $\rho_\epsilon = \tilde{\rho}(t = \epsilon^2/2)$ where $\tilde{\rho}$ is the solution of the heat equation with initial data ρ . Then ϵ is the width of the corresponding Gaussian filter. Figure 2 gives an example of such an image smoothing and edge enhancement by nonlinear diffusion. The function $f(\cdot)$ may serve as a penalty which forces the scale of images to stay close to



Figure 2: The noisy image on the left is successively smoothed by nonlinear diffusion. On the right the resulting smoothed image with enhanced edges is shown.

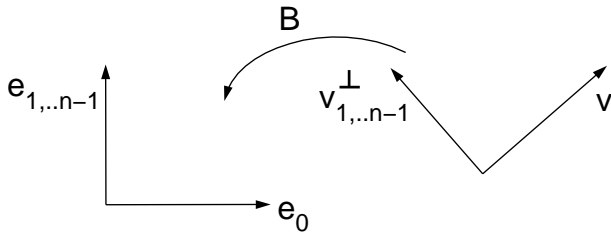


Figure 3: The coordinate transformation $B(v)$.

the initial image, e. g. choosing $f(\rho) = \gamma(\rho_0 - \rho)$ where γ is a positive constant.

Now we incorporate anisotropic diffusion. For a given vector field $v : \Omega \rightarrow \mathbb{R}^n$ we consider linear diffusion in the direction of the vector field and a Perona Malik type diffusion orthogonal to the field. Let us suppose that v is continuous and $v \neq 0$ on Ω . Then there exists a family of continuous orthogonal mappings $B(v) : \Omega \rightarrow SO(n)$ such that $B(v)v = \|v\|e_0$, where $\{e_i\}_{i=0,\dots,n-1}$ is the standard base in \mathbb{R}^n (cf. Fig. 3). We consider a diffusion matrix $A = A(v, \nabla \rho_\epsilon)$ and define

$$A(v, d) = B(v)^T \begin{pmatrix} \alpha(\|v\|) & \\ & G(d)\text{Id}_{n-1} \end{pmatrix} B(v)$$

where $\alpha : \mathbb{R}^+ \rightarrow \mathbb{R}^+$ controls the linear diffusion in vector field direction, i. e. along streamlines, and the above introduced edge enhancing diffusion coefficient $G(\cdot)$ acts in the orthogonal directions. Here Id_{n-1} is the identity matrix in dimension $n - 1$. We may either choose a linear function α or in case of a velocity field, which spatially varies over several orders of magnitude, we select a monotone function α (cf. Fig. 4) with

$$\alpha(0) > 0 \text{ and}$$

$$\lim_{s \rightarrow \infty} \alpha(s) = \alpha_{\max}.$$

In general it does not make sense to consider a certain initial image. As initial data ρ_0 we thus choose some random noise of an appropriate frequency range. This can for instance be generated running a linear isotropic diffusion simulation on a discrete white noise for a short time. Hence patterns will grow upstream and downstream, whereas the edges tangential to these patterns are successively enhanced. Still there is some diffusion perpendicular to the field which supplies us for evolving time with a scale of progressively coarser representation of the flow field. If we run the evolution for vanishing right hand side f the image contrast will unfortunately decrease due to the diffusion along streamlines. The asymptotic

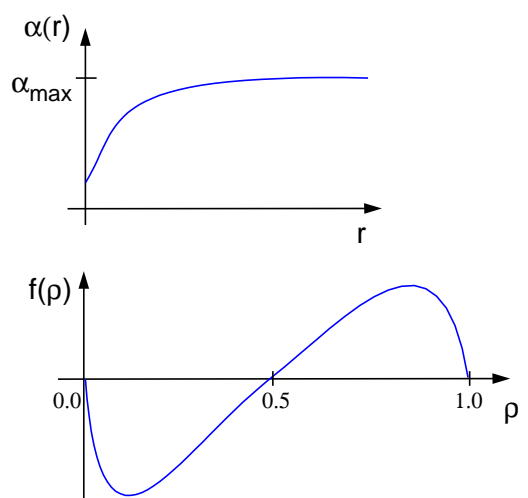


Figure 4: The graphs of the velocity dependent linear diffusion $\alpha(\cdot)$, respectively the scalar contrast enhancing right hand side $f(\cdot)$.

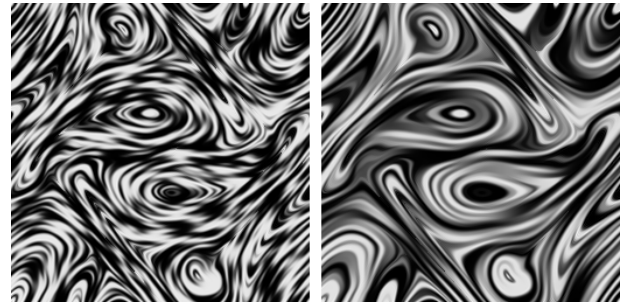


Figure 5: A vector field from a 2D magneto-hydrodynamics simulation (MHD) is visualized by nonlinear diffusion. A discrete white noise is considered as initial data. We run the evolution on the left for a small and on the right for a large constant diffusion coefficient α .

limit would turn out to be an averaged grey value. Therefore, we strengthen the image contrast during the evolution, selecting an appropriate function $f : [0, 1] \rightarrow \mathbb{R}^+$ (cf. Fig. 4) with

$$f(0) = f(1) = 0,$$

$$f > 0 \text{ on } (0.5, 1), \text{ and } f < 0 \text{ on } (0, 0.5).$$

If we - at the first glance - neglect the diffusive term in the equation, one realizes that perturbations below the average value 0.5 are pushed towards the zero value and accordingly values above 0.5 are pushed towards 1. Well-known maximum principles ensure that the interval of grey values $[0, 1]$ is not enlarged running the nonlinear diffusion. Here the first property of f is of great importance. Finally we end up with the method of nonlinear anisotropic diffusion to visualize complex vector fields. Thereby we solve the nonlinear parabolic problem

$$\frac{\partial}{\partial t} \rho - \text{div}(A(v, \nabla \rho_\epsilon) \nabla \rho) = f(\rho)$$

starting from some random initial image ρ_0 and obtain a scale of images representing the vector field in an intuitive way (cf. Fig. 5).

The corresponding variational formulation is obviously given by

$$(\partial_t \rho, \theta) + (A(v, \nabla \rho_\epsilon) \nabla \rho, \nabla \theta) = (f, \theta),$$

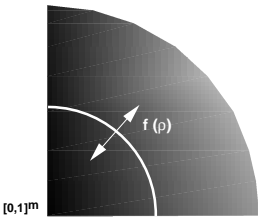


Figure 6: A sketch of the vector valued contrast enhancing function f which leads to asymptotic states $\rho(\infty, \cdot) \in \{0\} \cup (S^{m-1} \cap [0, 1]^m)$. Here, the components of the density are interpreted as blue respectively green color values. The arrows indicate the direction of contrast enhancement.

for all $\theta \in C^\infty(\Omega)$, where $(., .)$ denotes the L^2 product on the domain Ω . Our later finite element implementation will be based on this formulation by restriction to finite dimensional function spaces.

4 Coupled system of diffusion equations

If we ask for point wise asymptotic limits of the evolution, we expect an almost everywhere convergence to $\rho(\infty, \cdot) \in \{0, 1\}$ due to the choice of the contrast enhancing function $f(\cdot)$. Analytically 0.5 is a third, but unstable fix point of the dynamics. Thus numerically it will not turn out to be locally dominant. The space of asymptotic limits significantly influences the richness of the developing vector field aligned structures. We may ask how to further enrich the pattern which is settled by anisotropic diffusion. This turns out to be possible by increasing the set of asymptotic states. We no longer restrict ourselves to a scalar density ρ but consider a vector valued $\rho : \Omega \rightarrow [0, 1]^m$ for some $m \geq 1$ and a corresponding system of parabolic equations. The coupling is given by the nonlinear diffusion coefficient $G(\cdot)$ which now depends on the norm $\|\nabla \rho\|$ of the Jacobian of the vector valued density $\nabla \rho$ and the right hand side $f(\cdot)$. We define

$$f(\rho) = h(\|\rho\|)\rho$$

with $h(s) = \tilde{f}(s)/s$ for $s \neq 0$, where \tilde{f} is the old right hand side from the scalar case, and $h(0) = 0$. Furthermore we select an initial density which is now a discrete “white noise with values in $B_1(0) \cap [0, 1]^m$. Thus the contrast enhancing now pushes the point wise vector density ρ either to the 0 or to some value on the sphere sector $S^{m-1} \cap [0, 1]^m$ in \mathbb{R}^m (cf. Fig. 6). Again a straightforward application of the maximum principle ensures $\rho(t, x) \in S^{m-1} \cap [0, 1]^m$ for all t and $x \in \Omega$.

Figure 7 shows an example for the application of the vector valued anisotropic diffusion method applied to a 2D flow field from a MHD simulation convective flow field. Furthermore, Figure 8 shows results of this method applied to several time steps of a convective flow field. An incompressible Bénard convection is simulated in a rectangular box with heating from below and cooling from above. The formation of convection rolls will lead to an exchange of temperature. We recognize that the presented method is able to nicely depict the global structure of the flow field, including its saddle points, vortices, and stagnation points on the boundary. Figure 9 shows results for the same data sets obtained by line integral convolution (Here we used the implementation of Hege and Stalling [21]). Finally, Fig. 10 shows a different application to a porous media flow field.

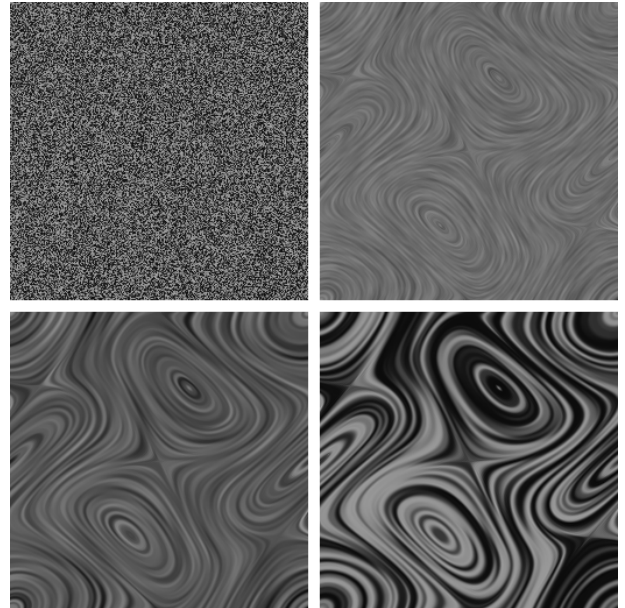


Figure 7: Different snapshots from the multiscale based on anisotropic diffusion are depicted for a 2D MHD simulation vector field. Here we consider a two dimensional diffusion problem and interpreted the resulting density as a color in a blue/green color space

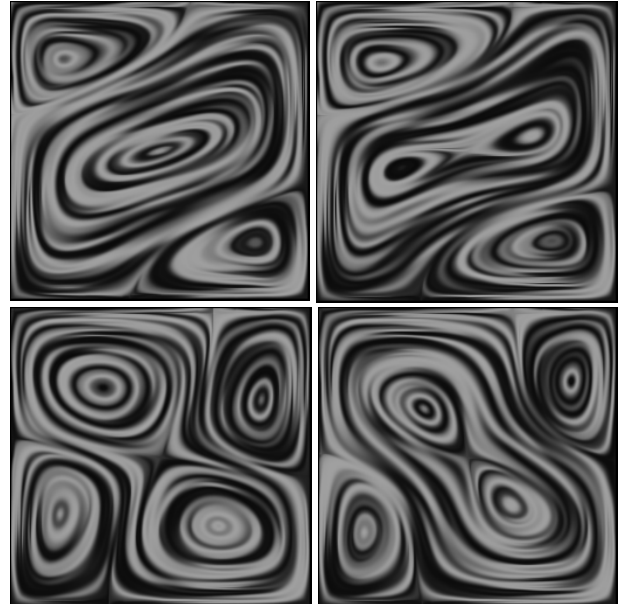


Figure 8: Convective patterns in a 2D flow field are displayed and emphasized by the method of anisotropic nonlinear diffusion. The images show the velocity field of the flow at different time steps. Thereby the resulting alignment is with respect to streamlines of this time dependent flow.

5 Application in 3D

The anisotropic nonlinear diffusion problem has been formulated in Section 3 for arbitrary space dimension. It results in a scale of vector field aligned patterns which we then have to visualize. In 2D this has already been done in a straightforward manner in the above figures. In 3D we have somehow to break up the volume and open up the view to inner regions. Otherwise we must confine ourselves with some pattern close to the boundary representing solely the shear flow.

Here a further benefit of the vector valued diffusion comes into operation. We know that for $m = 2$ the asymptotic limits - which differ from 0 - are in mean equally distributed on $S^1 \cap [0, 1]^2$. Hence, we reduce the informational content and focus on a ball shaped neighborhood $B_\delta(\omega)$ of a certain point $\omega \in S^1 \cap [0, 1]^2$. Now we can either look at isosurfaces of the function

$$\sigma(x) = \|\rho(x) - \omega\|^2,$$

where the isolevel δ^2 allows us to depict the boundary of the preimage of $B_\delta(\omega)$ with respect to the mapping ρ (cf. Fig. 11 and Fig. 12). Alternatively we might use volume rendering to visualize this type of sub volumes. A detailed discussion of the latter approach is beyond the scope of this paper.

6 Anisotropic diffusion on surfaces

In the above sections we have discussed anisotropic diffusion in vector field visualization on domains which are subsets of two- and three dimensional Euclidian space. In what follows we will outline how to carry over this methodology to display tangential vector fields on surfaces. Important examples are results from meteorological simulations, flow fields on streamsurfaces, or vector fields in differential geometry. The applications presented here will focus on the latter case and present multiscale textures on surfaces representing the principal directions of curvature. Based on the well established intrinsic differential calculus on manifolds [7], we can pick up the same diffusion problems with an appropriate reinterpretation of the operators. Thus, let us first briefly review the basic notation of manifolds, differential calculus and geometric diffusion. For a detailed introduction to geometry and differential calculus we refer to [7] and [5, Chapter 1]. For the sake of simplicity we assume our surfaces to be compact embedded manifolds without boundary. Thus we consider a smooth manifold \mathcal{M} , which we suppose to be embedded in \mathbb{R}^3 . Let $x : \Omega \rightarrow \mathcal{M}; \xi \mapsto x(\xi)$ be a coordinate map from an atlas of \mathcal{M} . For each point x on \mathcal{M} the embedded tangent space $T_x \mathcal{M}$ is spanned by the basis $\{\frac{\partial x}{\partial \xi_1}, \frac{\partial x}{\partial \xi_2}\}$. By $\mathcal{T}\mathcal{M}$ we denote the tangent bundle. On \mathcal{M} the metric $g(\cdot, \cdot)$ as a bilinear form on $\mathcal{T}\mathcal{M} \times \mathcal{T}\mathcal{M}$ is prescribed by the metric tensor $g = (g_{ij})_{ij}$ with

$$g_{ij} = \frac{\partial x}{\partial \xi_i} \cdot \frac{\partial x}{\partial \xi_j},$$

where \cdot indicates the scalar product in \mathbb{R}^3 . The inverse of g is denoted by $g^{-1} = (g^{ij})_{ij}$. Based on the metric we can define the integration of a function f on \mathcal{M} . We split up an integral over \mathcal{M} into separate integrals over subsets, which are in the image $x(\Omega)$ of some coordinate map x and define

$$\int_{x(\Omega)} f := \int_{\Omega} f(x(\xi)) \sqrt{\det g} d\xi.$$

Integrating either a product of two functions f, g on \mathcal{M} or the product of two vector fields v, w on $\mathcal{T}\mathcal{M}$ we obtain the following scalar

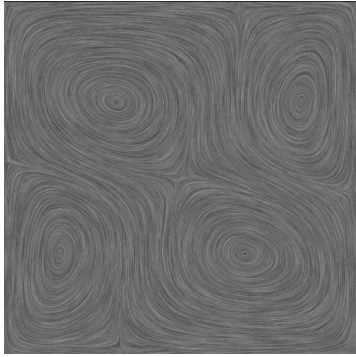


Figure 9: LIC image generated for one of the data sets that have already been processed in Fig. 8 by nonlinear diffusion (cf. lower left image in Fig. 8).

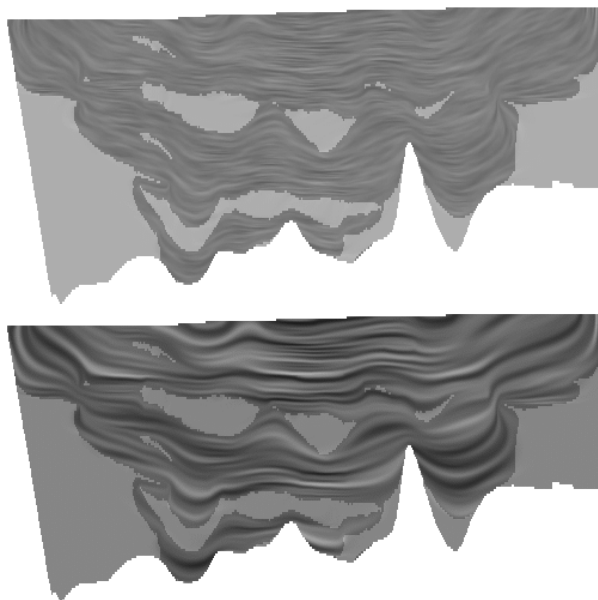


Figure 10: Field aligned diffusion clearly outlines the principle features of a porous media flow in the vicinity of a salt dome. Lenses of lower permeability force the flow to pass through narrow bridges. We depict two time steps of the diffusion process.

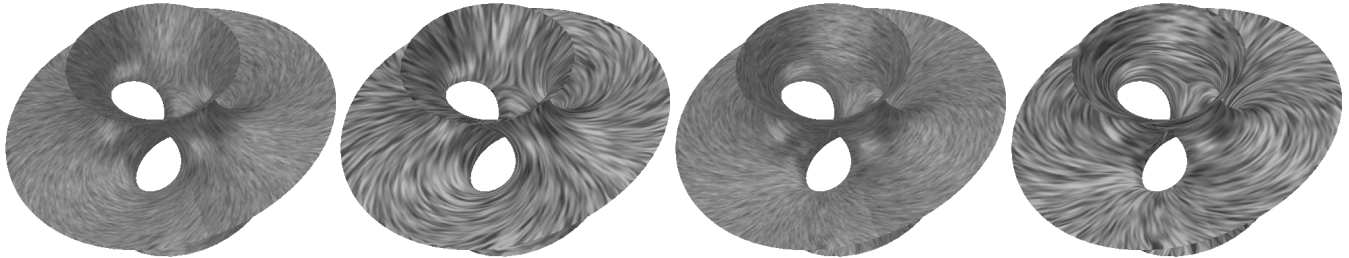


Figure 13: The principal directions of curvature are visualized by anisotropic diffusion on a minimal surface.

products on $C^0(\mathcal{M})$ and $C^0(\mathcal{T}\mathcal{M})$ respectively:

$$(f, g)_{\mathcal{M}} := \int_{\mathcal{M}} f g \, dx,$$

$$(v, w)_{\mathcal{T}\mathcal{M}} := \int_{\mathcal{M}} g(v, w) \, dx.$$

Next, we have to introduce the fundamental intrinsic gradient and divergence operators on \mathcal{M} . The gradient $\nabla_{\mathcal{M}} f$ of f is defined as the representation of df with respect to the metric g . We obtain in coordinates

$$\nabla_{\mathcal{M}} f = \sum_{i,j} g^{ij} \frac{\partial(f \circ x)}{\partial \xi_j} \frac{\partial x}{\partial \xi_i}.$$

Furthermore, we define the divergence $\operatorname{div}_{\mathcal{M}} v$ for a vector field $v \in \mathcal{T}\mathcal{M}$ as the dual operator of the gradient by

$$\int_{\mathcal{M}} \operatorname{div}_{\mathcal{M}} v \phi \, dx := - \int_{\mathcal{M}} g(v, \nabla_{\mathcal{M}} \phi) \, dx$$

for all $\phi \in C_0^\infty(\mathcal{M})$.

Finally, with these differential operators at hand we can discuss a general and intrinsic diffusion on a manifold in analogy to diffusion in Euclidian space: We ask for a solution $\rho : \mathbb{R}_0^+ \times \mathcal{M} \rightarrow \mathbb{R}$ of the parabolic equation

$$\frac{\partial}{\partial t} \rho - \operatorname{div}_{\mathcal{M}}(A \nabla_{\mathcal{M}} \rho) = f(\rho)$$

on $\mathbb{R}_0^+ \times \mathcal{M}$ for given initial data $\rho(0, \cdot) = \rho_0$ on \mathcal{M} . Here we suppose A to be some positive definite symmetric endomorphism on $\mathcal{T}\mathcal{M}$. Testing with any function $\theta \in C^\infty(\mathcal{M}(t))$ and integrating over \mathcal{M} we obtain the variational formulation

$$(\partial_t \rho, \theta)_{\mathcal{M}} + (A \nabla_{\mathcal{M}} \rho, \nabla_{\mathcal{M}} \theta)_{\mathcal{T}\mathcal{M}} = (f(\rho), \theta)_{\mathcal{M}}.$$

Now we consider our actual goal, which is the generation of a texture by nonlinear anisotropic diffusion to represent a given vector field $v \in \mathcal{T}\mathcal{M}$ on the surface. Thus, we suppose A to depend on the vector field v and the norm of the gradient of a convoluted intensity ρ_ϵ :

$$A = A(v, \|\nabla_{\mathcal{M}} \rho_\epsilon\|)$$

For no vanishing v let $w \in \mathcal{T}_x \mathcal{M}$ be some unit vector normal to v , i. e. $g(v, w) = 0$. Hence, $\{\frac{v}{\|v\|}, w\}$ is a basis of $\mathcal{T}_x \mathcal{M}$ and with respect to this basis we define as before in the Euclidian case

$$A(v, d) = \begin{pmatrix} \alpha(\|v\|) & \\ & G(d) \end{pmatrix}.$$

As right hand side $f(\cdot)$ we pick up the one already introduced in Section 3 and again assume ρ_0 to be a random noise, either scalar or vector valued, but now prescribed on the surface \mathcal{M} . Furthermore, we have to give a suitable definition of the regularizing presmoothing to obtain ρ_ϵ from the original intensity ρ . Again we proceed in analogy to the Euclidian case and define ρ_ϵ as the result of the above diffusion problem with $A = \operatorname{Id}$ at time $t = \frac{\epsilon^2}{2}$ and for initial data ρ .

Finally, the resulting family $\{\rho(t)\}_{t \geq 0}$ of intensities on \mathcal{M} gives a multiscale of representations of the given vector field v . Figure 13,14 show results on different surfaces. We consider the principal directions of curvature as tangential vector fields on which we apply the anisotropic diffusion method. On the underlying triangular grids, the shape operator, whose eigenvalues are the principal curvatures, is approximated as follows. Locally we regard a single triangle T and all the neighboring triangles which have a non zero intersection with T as a graph over the plane containing T and calculate the L^2 projection of this piecewise linear graph onto the set of quadratic graphs which are tangential to the plane. Then we evaluate the constant shape operator on this graph. Let us emphasize that the L^2 projection is always defined, although the local graph property of the triangular grid might not hold in certain degenerate cases.

7 Discretization in 2D and 3D

In what follows we discuss the discretization and implementation of the field aligned diffusion method. We will first focus on domains in 2D and 3D Euclidian space. For this purpose a finite element discretization in space and a semi implicit backward Euler or second order Crank Nicolson scheme in time are considered. Here we have restricted ourselves to regular grids in 2D and 3D generated by recursive subdivision. On these grids we consider bilinear, respectively trilinear finite element spaces. Numerical integration is based on the lumped masses product $(\cdot, \cdot)^h$ [23] for the L^2 product (\cdot, \cdot) in the variational formulation and a one point quadrature rule for the bilinear form $(A \nabla \cdot, \nabla \cdot)$. Semi implicit means for the schemes considered here that the nonlinearity $A(\cdot)$ is evaluated at the old time. Finally, in each step of the discrete evolution we have to solve a single system of linear equations. We obtain for a backward Euler discretization

$$(M^k + \tau L^k(A^k))\bar{\rho}^{k+1} = M^k \bar{\rho}^k + \tau M^k \bar{f}^k.$$

Here $\bar{\rho}^k = (\bar{\rho}_i^k)$ is the vector of nodal intensity values at time $t^k = k\tau$, where τ is the selected time step size. Furthermore, if we denote the “hat shaped” multilinear basis functions by Φ_i and the diffusion tensor with respect to the discrete intensity at time t^k by

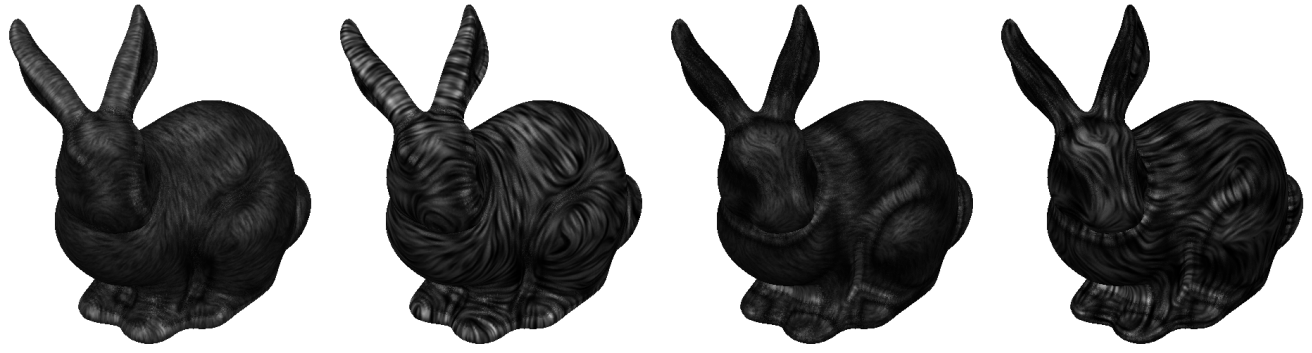


Figure 14: For both principal directions of curvature different timesteps of the anisotropic diffusion are displayed on the surface of a presmoothed Stanford bunny. In addition the corresponding principle curvature values are color coded.

$$A^k,$$

$$\begin{aligned} M^k &:= \left((\Phi_i, \Phi_j)^h \right)_{ij} \\ L^k(A^k) &:= \left((A^k \nabla \Phi_i, \nabla \Phi_j) \right)_{ij} \end{aligned}$$

are the lumped mass matrix and nonlinear stiffness matrix respectively. Finally, the components of the right hand side \bar{f}^k are evaluated by $(\bar{f}^k)_i = f(\bar{\rho}_i^k)$.

The global matrices M^k and $L^k(A^k)$ are assembled from local matrices m^E and l^E with respect to a single element. There entries correspond to all pairings of local basis functions. Due to the applied lumped mass integration we immediately verify

$$m_{ij}^E = \frac{1}{2^n} \delta_{ij} |E|$$

where $|E|$ is the volume of the rectangular element E and δ_{ij} the usual Kronecker symbol. For the nonlinear stiffness matrix we obtain

$$\begin{aligned} l_{ij}^E(A) = |E| &\left[\alpha(\|V\|) \left(\nabla \Phi^i \cdot \frac{V}{\|V\|} \right) \left(\nabla \Phi^j \cdot \frac{V}{\|V\|} \right) + \right. \\ &G(D) \left(\nabla \Phi^i - \nabla \Phi^i \cdot \frac{V}{\|V\|^2} V \right) \\ &\left. \cdot \left(\nabla \Phi^j - \nabla \Phi^j \cdot \frac{V}{\|V\|^2} V \right) \right]. \end{aligned}$$

where $V = v(c_E)$ for the center of mass c_E of E , D the gradient of the presmoothed discrete intensity at c_E , and $\{\Phi^i\}_i$ the set of local basis functions.

In each time step the computation of the prefiltered intensity vector $\bar{\rho}_\epsilon^n$ is based on a single implicit time step $\epsilon^2/2$ for the corresponding discrete heat equation scheme with respect to initial data $\bar{\rho}^n$.

In our implementation the regular grids are procedurally interpreted as quadtrees, respectively octrees [19]. Finally no matrix is explicitly stored. The necessary matrix multiplications in the applied iterative CG solver are performed in successive tree traversals. Hierarchical BPX type [3] preconditioning is used to accelerate the convergence of the linear solver. The computation of a single time step on a 257^2 grid performed on a Silicon Graphics workstation with an R10000 processor requires 1.2 seconds. Computing time in 3D is currently much more expensive. But there is still a great potential to speed up the algorithm considerably, for instance by taking into account better ordering strategies for the unknowns which correspond to the anisotropy. This will be exploited in the future.

Furthermore, the code is prepared to incorporate spatial grid adaptivity if possible (cf. Fig. 17).

8 Discretization on surfaces

The discretization of the proposed anisotropic diffusion method on surfaces is completely analogous to the above Euclidian case. We only have to replace the discrete differential operators and bilinear forms by their intrinsic geometric counterparts. We suppose the surface \mathcal{M} to be approximated with a sufficiently fine triangular grid \mathcal{M}_h consisting of nondegenerate triangles T with maximal diameter h . Thus, we only focus on the computation of the local mass matrix m^T and the local nonlinear stiffness matrix $l^T(A)$ respectively. We obtain again by lumped mass integration

$$m_{ij}^T = \frac{1}{3} \delta_{ij} |T|$$

where $|T|$ is the area of the triangle T . Next, let us consider for every triangle T the reference triangle $\hat{T} \subset \mathbb{R}^2$ with independent variables ξ_1, ξ_2 and nodes $\xi^0 = (0, 0)$, $\xi^1 = (1, 0)$, and $\xi^2 = (0, 1)$. Then an affine coordinate mapping X maps \hat{T} onto T and its nodes ξ^i onto the corresponding nodes P^i of T on the discrete surface in \mathbb{R}^3 . Hence the corresponding metric tensor is as in the continuous case given by $g_{ij} = \frac{\partial X}{\partial \xi_i} \cdot \frac{\partial X}{\partial \xi_j}$, where $\frac{\partial X_k}{\partial \xi_i} = P_k^i - P_k^0$. Hence we can evaluate gradients of the linear basis functions Φ^l corresponding to the nodes P^l by

$$\nabla_{\mathcal{M}_h} \Phi^l = \sum_{i,j} g^{ij} \frac{\partial \Phi^l}{\partial \xi_j} (P^i - P^0),$$

where the derivatives of Φ^l with respect to the reference coordinates ξ are

$$\begin{pmatrix} \frac{\partial \Phi^l}{\partial \xi_1} \\ \frac{\partial \Phi^l}{\partial \xi_2} \end{pmatrix} = \begin{pmatrix} -1 \\ -1 \end{pmatrix}, \begin{pmatrix} 1 \\ 0 \end{pmatrix}, \begin{pmatrix} 0 \\ 1 \end{pmatrix}.$$

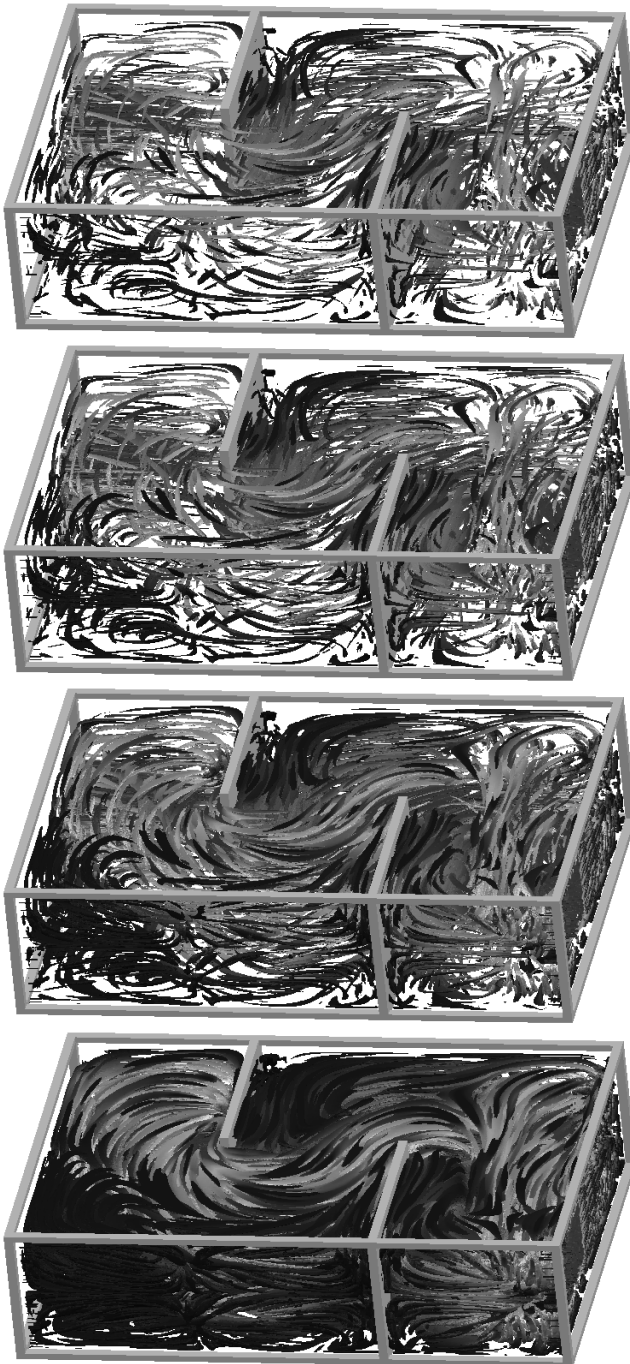


Figure 11: The incompressible flow in a water basin with two interior walls and an inlet (on the left) and an outlet (on the right) is visualized by the anisotropic nonlinear diffusion method. Isosurfaces show the preimage of $\partial B_\delta(\omega)$ under the vector valued mapping ρ for some point ω on the sphere sector. From top to bottom the radius δ is successively increased. A color ramp blue–green–red indicates an increasing absolute value of the velocity. The diffusion is applied to initial data which is a relatively coarse grain random noise.

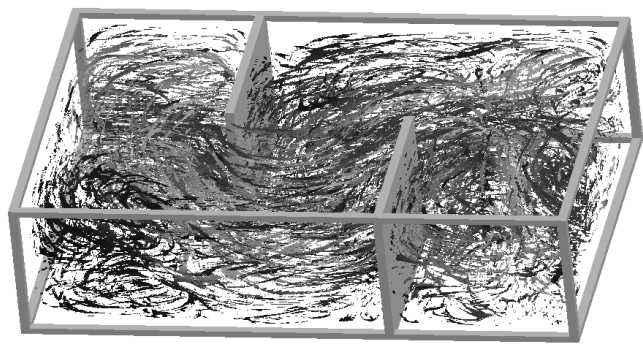


Figure 12: Nonlinear anisotropic diffusion applied to the same 3D data set as in Fig. 11, but with a fine grain white noise as initial data.

Finally we calculate the local nonlinear stiffness matrix

$$l_{ij}^T(A) = |T| \left[\alpha(\|V\|) \left(\nabla_{\mathcal{M}_h} \Phi^i \cdot \frac{V}{\|V\|} \right) \left(\nabla_{\mathcal{M}_h} \Phi^j \cdot \frac{V}{\|V\|} \right) + G(D) \left(\nabla_{\mathcal{M}_h} \Phi^i - \nabla_{\mathcal{M}_h} \Phi^i \cdot \frac{V}{\|V\|^2} V \right) \cdot \left(\nabla_{\mathcal{M}_h} \Phi^j - \nabla_{\mathcal{M}_h} \Phi^j \cdot \frac{V}{\|V\|^2} V \right) \right].$$

where $V = v(c_T)$ for the center of mass c_T of T , D the geometric gradient of the presmoothed discrete intensity on T and “.” still indicates the scalar product in \mathbb{R}^3 .

9 Comparison to Other Methods

So far we have introduced a novel approach which provides us with an intuitive understanding of complex vector fields. We have discussed a variety of important properties and advantages. Let us now rank this method among other visualization methods and compare it with different techniques. Here we especially pick up the line integral convolution method and the spot noise approach.

For stationary vector fields we obtain similar results by all methods. Thin field aligned patterns are generated. Line integral convolution leads to comparable results with the essential difference that the PDE based method carries a nice scale space property. I. e. evolving a longer time in the anisotropic diffusion method we obtain a successive coarsening of the resulting pattern representing the vector field.

Furthermore, in a restricted sense, line integral convolution (LIC) and spot noise can be regarded as special cases of the anisotropic nonlinear diffusion method. LIC with Gaussian filter kernel can be identified as the asymptotic limit of the latter method for a concentration of the edge enhancing function $G(\cdot)$ at 0. Other filter kernel shapes correspond to different, in general non linear diffusion processes along streamlines. Further on, generating a single deformed spot on the computational domain like proposed in [6] can be regarded as an early time step in the diffusion starting with initial data, that is a characteristic function of a circular disk. If we release a bunch of such disks as initial data in such a way that the evolving patterns do not overlap, then the resulting image is comparable to spot noise. Thus, the original spot noise technique can be regarded as a parallel version of short time diffusive vector field visualization.

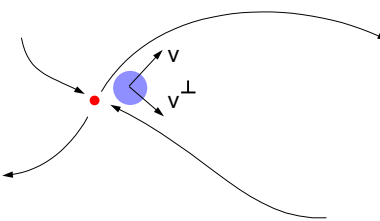


Figure 15: A sketch of the four sectors at a critical point, the initial spot for the diffusion calculation and the oriented system $\{v, v^\perp\}$.

10 Towards Flow Segmentation

The above applications already show the capacity of the anisotropic nonlinear diffusion method to outline the flow structure not only locally. Indeed especially for larger evolution times in the diffusion process the topological skeleton of a vector field becomes clearly visible. We will now investigate a possible flow segmentation by means of the anisotropic diffusion. Let us restrict to the two dimensional case of an incompressible flow with vanishing velocity v at the domain boundary $\partial\Omega$. Then topological regions are separated by homoclinic, respectively heteroclinic orbits connecting critical points in the interior of the domain and stagnation points on the boundary. Critical points, by definition points with vanishing velocity $v = 0$, may either be saddle points or vortices. Furthermore we assume critical points to be non degenerate, i. e. ∇v is regular. Saddle points are characterized by two real eigenvalues of ∇v with opposite sign, whereas at vortices we obtain complex conjugate eigenvalues with vanishing real part. Stagnation points on $\partial\Omega$ are similar to saddles. For details we refer to [11]. In each topological region there is a family of periodic orbits close to the heteroclinic, respectively homoclinic orbit. This observation gives reason for the following segmentation algorithm. At first, we search for critical points in Ω and stagnation points on $\partial\Omega$. We calculate the directions which separate the different topological regions. In case of saddle points these are the eigenvectors of ∇v . Next, we successively place an initial spot in each of the sectors and perform an appropriate field aligned anisotropic diffusion. Let us suppose that a single sector is spanned by vectors $\{s_+, s_-\}$ where the sign \pm indicates incoming and outgoing direction. The method presented in Sect. 3 would lead to a closed pattern along one of the above closed orbits for time t large enough. To fill out the interior region we modify the diffusion as follows. Up to now the Perona Malik diffusions enhances edges of the current image in both directions normal to the velocity. Henceforth we select an orientation for a “one sided diffusion (cf. Fig. 15). I. e. we select a unique normal v^\perp to v and consider the diffusion matrix

$$A(v, \nabla \rho_\epsilon) = B(v)^T \begin{pmatrix} \alpha & \\ & G((\nabla \rho_\epsilon \cdot v^\perp)_+) \end{pmatrix} B(v),$$

where α is a positive constant and $(s)_+ := \max\{s, 0\}$. Furthermore we consider a non negative, concave function $f : \mathbb{R}_0^+ \rightarrow \mathbb{R}_0^+$ with $f(0), f(1) = 0$ as a source term in the diffusion equation. If the orientation of $\{s_+, s_-\}$ coincides with that of $\{v, v^\perp\}$, then linear diffusion in the direction towards the interior will fill up the complete topological region. A segmentation of multiple topological regions at the same time is possible, if we carefully select the sectors to release initial spots. Figure 16 shows different time steps of the segmentation applied to a convective incompressible flow. So far we have seen that anisotropic diffusion has strong provisions for flow segmentation as well. In a certain sense we thereby identify the complement of what is usually extracted in topology recognition. An outstanding advantage of the new method is its numerical stability and its self sharpening effect due to the edge enhancing

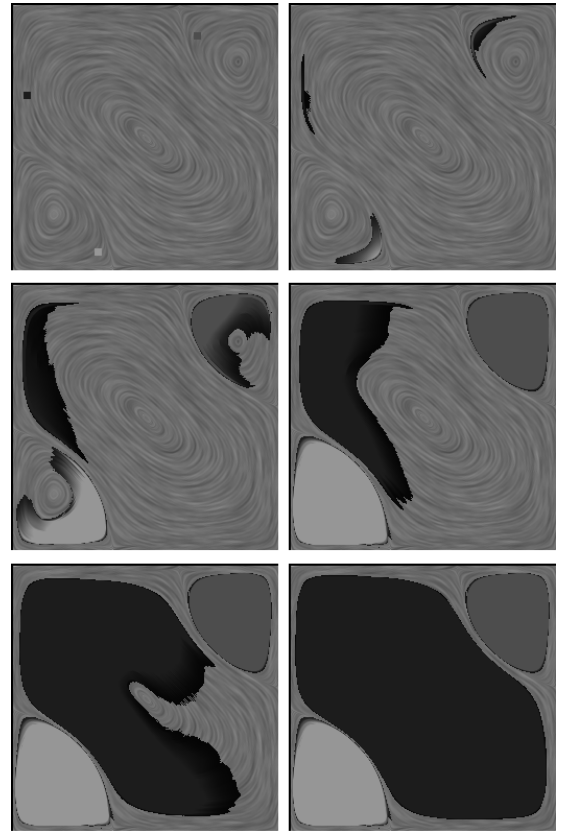


Figure 16: Nonlinear diffusion segmentation is applied to a velocity field from a Bénard convection. Several time steps are shown starting from initial seed spots in critical point sectors. Here we have placed these seeds as close as possible in terms of the grid size in the sectors spanned by the eigenvalues of the Jacobian of the velocity. Only to emphasize the evolution process a single greyscale image from the diffusion calculation (cf. Fig. 8) is underlying the sequence of segmentation time steps.

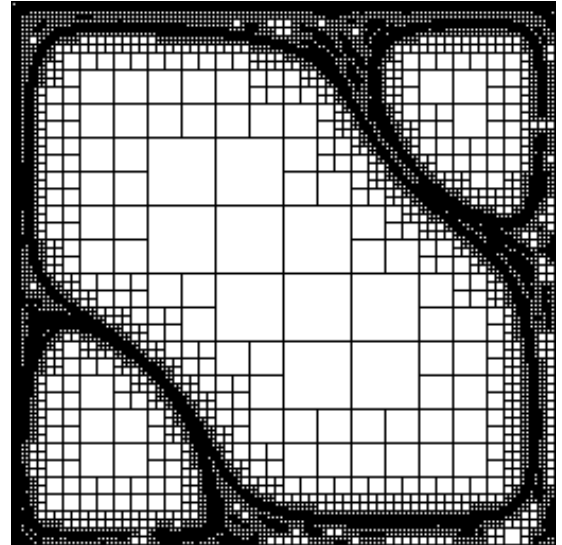


Figure 17: The adaptive quadtree on which we approximate the segmentation function ρ at a certain time step.

strategy. We pay for this by a higher computational complexity. If we apply a standard implementation on a uniform grid of size n^2 , the segmentation cost is at least $O(n^2)$ compared to an $O(n)$ count of grid cells met by the direct ODE integration to compute the homoclinic and heteroclinic orbits corresponding to the critical points. Figure 17 shows an adaptive quadtree, which allows the same resolution quality for the segmentation function ρ as on a full grid, but now at a much lower cost. Thereby, we consider a piecewise linear and continuous finite element space on the adaptive quadtree.

11 Conclusions

We have introduced a new method based on the solution of a nonlinear anisotropic diffusion problem for the post processing of vector data. The method can be applied on 2D or 3D domains as well as on two-dimensional surfaces embedded in \mathbb{R}^3 . From a mathematical point of view one of the major advantages is, that it is based on a physically intuitive continuous model, i. e. streamline aligned diffusion. Most of the properties can be discussed on this level. Finally, it is discretized in an appropriate way making use of recent and efficient numerical algorithms.

From the authors' point of view exciting future research directions are further investigations of flow visualization in 3D. Especially the exploiting of adaptive finite element paradigms and ordering strategies for the unknowns will be key issues to reduce the computing costs.

Furthermore, a visualization approach based on anisotropic diffusion and applicable for time dependent vector fields is a challenging topic. Finally, the anisotropic diffusion flow segmentation also carries provisions for the identification of interesting flow regions in 3D, such as recirculation zones and vortex cores.

Further results and the algorithm running on an $n \times m$ 2D vector array is available as a source code at the URL:

http://wwwIAM.uni-bonn.de/FktAna_NumMath/Num_Vis/projekte/flow_visualization/

Acknowledgement

The authors would like to acknowledge Karol Mikula and Jarke van Wijk for inspiring discussions and many useful comments on image processing and flow visualization. Furthermore they thank Eberhard Bänsch from Bremen University, Klaus Johannsen from Stuttgart University, Konrad Polthier from the Technical University at Berlin and Wolfram Rosenbaum from Bonn for providing the incompressible flow data sets, the porous media simulation data, the minimal surface data, and the MHD simulation data sets.

References

- [1] L. Alvarez, F. Guichard, P.-L. Lions, and J.-M. Morel. Axioms and fundamental equations of image processing. *Arch. Ration. Mech. Anal.*, 123 (3):199–257, 1993.
- [2] J. Becker and M. Rumpf. Visualization of time-dependent velocity fields by texture transport. In *Proceedings of the Eurographics Scientific Visualization Workshop '98*. Springer, 1998.
- [3] J. Bramble, J. Pasciak, and J. Xu. Parallel multilevel preconditioners. *Math. of Comp.*, 55:1–22, 1990.
- [4] B. Cabral and L. Leedom. Imaging vector fields using line integral convolution. In J. T. Kajiya, editor, *Computer Graphics (SIGGRAPH '93 Proceedings)*, volume 27, pages 263–272, Aug. 1993.
- [5] I. Chavel. *Eigenvalues in Riemannian Geometry*. Academic Press, 1984.
- [6] W. C. de Leeuw and J. J. van Wijk. Enhanced spot noise for vector field visualization. In *Proceedings Visualization '95*, 1995.
- [7] M. P. do Carmo. *Riemannian Geometry*. Birkhäuser, Boston–Basel–Berlin, 1993.
- [8] G. Dziuk. Finite elements for the beltrami operator on arbitrary surfaces. In *Partial differential equations and calculus of variations, Lect. Notes Math. 1357*, 1988.
- [9] G. Dziuk. An algorithm for evolutionary surfaces. *Numer. Math.*, 58:603–611, 1991.
- [10] L. Forsslund. Visualizing flow over curvilinear grid surfaces using line integral convolution. In *Proceedings IEEE Visualization '94*, pages 240–246, 1994.
- [11] J. L. Helman and L. Hesselink. Visualizing Vector Field Topology in Fluid Flows. *IEEE G&A*, 11 (3):36–46, 1991.
- [12] V. Interrante and C. Grosch. Strategies for effectively visualizing 3d flow with volume lic. In *Proceedings Visualization '97*, pages 285–292, 1997.
- [13] J. Kačur and K. Mikula. Solution of nonlinear diffusion appearing in image smoothing and edge detection. *Appl. Numer. Math.*, 17 (1):47–59, 1995.
- [14] Kawohl, B. and Kutev, N. Maximum and comparison principle for one-dimensional anisotropic diffusion. *Math. Ann.*, 311 (1):107–123, 1998.
- [15] M.-H. Kiu and D. C. Banks. Multi-frequency noise for lic. In *Proceedings Visualization '96*, 1996.
- [16] N. Max and B. Becker. Flow visualization using moving textures. In *Proceedings of the ICASE/LaRC Symposium on Time Varying Data, NASA Conference Publication 3321*, pages 77–87, 1996.
- [17] N. Max, R. Crawfis, and C. Grant. Visualizing 3D Velocity Fields Near Contour Surface. In *Proceedings of IEEE Visualization '94*, pages 248–254, 1994.
- [18] P. Perona and J. Malik. Scale space and edge detection using anisotropic diffusion. In *IEEE Computer Society Workshop on Computer Vision*, 1987.
- [19] T. Preußer and M. Rumpf. Anisotropic nonlinear diffusion in flow visualization. In *Proceedings Visualization 1999*, 1999.
- [20] H.-W. Shen and D. L. Kao. Uflic: A line integral convolution algorithm for visualizing unsteady flows. In *Proceedings Visualization '97*, pages 317–322, 1997.
- [21] D. Stalling and H.-C. Hege. Fast and resolution independent line integral convolution. In *SIGGRAPH 95 Conference Proceedings*, pages 249–256. ACM SIGGRAPH, Addison Wesley, Aug. 1995.
- [22] D. Stalling, M. Zöckler, and H.-C. Hege. Fast display of illuminated field lines. *IEEE Transactions on Visualization and Computer Graphics*, 3(2), Apr.–June 1997. ISSN 1077-2626.
- [23] V. Thomée. *Galerkin - Finite Element Methods for Parabolic Problems*. Springer, 1984.

- [24] G. Turk and D. Banks. Image-guided streamline placement. In *Computer Graphics (SIGGRAPH '96 Proceedings)*, 1996.
- [25] J. J. van Wijk. Spot noise-texture synthesis for data visualization. In T. W. Sederberg, editor, *Computer Graphics (SIGGRAPH '91 Proceedings)*, volume 25, pages 309–318, July 1991.
- [26] J. J. van Wijk. Flow visualization with surface particles. *IEEE Computer Graphics and Applications*, 13(4):18–24, July 1993.
- [27] J. J. van Wijk. Implicit stream surfaces. In *IEEE Visualization '93*, pages 245–252, 1993.
- [28] J. Weickert. *Anisotropic diffusion in image processing*. Teubner, 1998.